COMMUNICATION

Layer-polarization-engineered ferroelectricity and anomalous valley hall effects in a van der Waals bilayer†

Nini Guo,[a] Jie Li,[b] Huijie Lian,[a] Shu Wang,[b] Yi Sun,*[c] Xiaojing Yao [ID] *[a] and Xiuyun Zhang [ID] *[b]

Layertronics, engineering the electronic properties through the layer degree of freedom, has attracted considerable attention due to its promising applications in next-generation spintronic technologies. Here, by coupling sliding ferroelectricity with A-type antiferromagnetism, we demonstrate a mechanism for layer-polarization-engineered electronic property through symmetry analysis based on the tight-binding (TB) model. It is found that breaking the inversion symmetry and time-inversion symmetry in the model gives rise to ferroelectricity and a layer-polarized anomalous valley Hall effect. Crucially, this valley polarization is ferroelectrically switchable, enabling non-volatile electrical control of the layer-resolved Berry curvature. Using first-principles calculations, this mechanism and phenomenon are verified in the multiferroic bilayer Janus RuClF. Our findings provide a promising platform for 2D bilayer materials, which hold great potential for applications in nanoelectronic and spintronic devices.

New concepts

Two-dimensional van der Waals (vdW) structures provide new flexibility for manipulating physical properties. Combining the tight binding model and first-principles calculations, we propose a mechanism for manipulating layer-polarized ferroelectricity and ferrovalleys in the A-type antiferromagnetic bilayer system through the interlayer sliding and interlayer exchange interactions. It is revealed that the ferroelectrically controllable layer-polarized anomalous valley Hall effect (AVHE) can be achieved by F–F interlayer termination in bilayer RuClF. Moreover, the electronic properties of the RuClF bilayer can be changed by different stacking configurations.

1. Introduction

In recent years, the discovery of various ferroic materials, whose properties are driven by different degrees of freedom of electron orbitals, has allowed advanced applications in information processing, spintronics, valleytronics, and electronics.[1] For example, the (anti)ferromagnetic candidates utilizing the spin degree of freedom are crucial in spintronic devices, where spin-aligned ferromagnetic (FM) materials can be used for spin-directed data storage in magnetic random access memory devices (MRAMs), and spin-antiparallel antiferromagnetic (AFM) materials offer high stability,

ultra-high speeds, and low-power-consumption spin transport properties. Ferrovalley (FV) materials are complementary to modern semiconductor technology, utilizing the valley degree of freedom to encode and process information.[2] Ferroelectric (FE) materials are also important in nonvolatile memory devices,[3] field-effect transistors,[4] *etc.*, by spontaneously generating an electric polarization. Additionally, multiferroic materials,

[a] College of Physics and Hebei Advanced Thin Films Laboratory, Hebei Normal University, Shijiazhuang 050024, China. E-mail: xjyao@hebtu.edu.cn

[b] College of Physics Science and Technology & Microelectronics Industry Research Institute, Yangzhou University, Yangzhou 225002, China. E-mail: xyzhang@yzu.edu.cn

[c] School of Electronic Engineering, Jiangsu Vocational College of Electronics and Information, Huaian 223003, China. E-mail: sunyi@jsei.edu.cn

† Electronic supplementary information (ESI) available. See DOI: https://doi.org/10.1039/d5nh00215j

Our first paper was published in Nanoscale Horizons in 2022 and we have contributed two papers to this journal to date. We are honoured to have the opportunity to collaborate with such an excellent journal in our research area. We will continue to collaborate with the journal to report on our significant research advances, such as the design of two-dimensional materials with rich magnetic and topological properties, as well as their potential applications. Congratulations and best wishes on the 10th anniversary of Nano-Horizon.

Xiuyun Zhang

which couple two or more types of ferroic order parameters, are of significant interest due to their multiple physical properties.[5] However, most intrinsic candidates are found to favor a single ferroic order due to the difficulty in balancing their origin mechanisms, maintaining structural stability as well as experimental feasibility, and so on.[6,7] Even for single ferroic materials, many suffer from the deficiencies that limit their practical applications, such as the non-spontaneous character of in-plane magnetization,[8] spin degeneration,[9] and lower magnetic transition temperature (T_C).[10]

Alternatively, two-dimensional (2D) van der Waals (vdW) homo-/hetero-bilayer or few-layer structures provide new flexibility for manipulating the physical properties by adjusting the vdW stacking, interlayer distance, and through atom or molecule intercalation, etc.[11–17] Firstly, varying the interlayer distance of vdW bilayers can assist in tuning the interlayer magnetic orders and electronic properties. For example, bilayer transition metal dichalcogenides, TMX_2 (TM = V, Cr, Mn; X = S, Se, Te), prefer interlayer AFM ordering at shorter interlayer distances and FM ordering at longer interlayer distances. The AFM–FM transition is governed by the competition between Pauli repulsion in the interlayer region and kinetic-energy gain across the bilayer.[18,19] The $MnPS_3/MnCl_3$ heterostructure undergoes transitions from semiconductor to metal to half-metal as the interlayer distance decreases.[20] Secondly, stacking or twisting is another effective method to modulate the electron correlation properties.[21–28] For example, $MnBr_3$ bilayers exhibit a high-Chern-number quantum anomalous Hall (QAH) state when stacked in the AB style, whereas the application of external electrostatic fields or circularly polarized light induces the layer Hall effect in the AC-stacked layer.[13] Switchable room-temperature out-of-plane electric polarization can be induced by changing the stacking order in the hexagonal BN bilayer.[22] Additionally, valley polarizations associated with twist angle and stacking configurations have been found for the WSe_2/WS_2 heterostructure[28] and the YI_2 bilayer.[29] Although these layered 2D materials exhibit a wealth of physical properties and modulation characteristics, there are still many unknowns to be explored in terms of the interlayer interactions and their impact on new physical phenomena. In particular, the interaction between sliding ferroelectricity and A-type antiferromagnetism in bilayer systems may lead to a series of unique physical effects.

In this study, we propose a mechanism to manipulate layer-polarized ferroelectricity and ferrovalley in the A-type AFM bilayer system through the interlayer sliding and interlayer exchange interactions. We first demonstrate this mechanism through the tight-binding (TB) model and then realize it in the bilayer Janus RuClF. By sliding the F–F oriented bilayers, ClRuF–FRuCl, the ferroelectrically controllable layer-polarized anomalous valley Hall effect (AVHE) can be achieved. The Cl–F facing bilayer, FRuCl–FRuCl, is a bipolar magnetic half-metal (BMHM), in which the spin-up and spin-down electrons in the upper and lower layers are conductive. The Cl–Cl-oriented FRuCl–ClRuF exhibits antiferrovalley behavior with a valley polarization of 300 meV in the RuClF sublayer.

2. Computational methods

All density functional theory (DFT) calculations were carried out within the Vienna Ab initio Simulation Package (VASP).[30,31] The exchange correlation interaction was characterized by the general gradient approximation (GGA) with the Perdew–Burke–Ernzerhof (PBE) functional.[32,33] The interaction between ion nuclei and valence electrons was described by the projector-augmented wave potential (PAW) method;[34] the energy cut-off for the plane-wave basis set was set as 500 eV. The vacuum spaces were set larger than 15 Å to avoid the physical interactions caused by periodic boundary conditions, and the vdW interaction in bilayer RuClF was considered using the DFT-D2 method.[35] To consider the Coulomb interaction and exchange interactions of the Ru-d electrons, the GGA+U method with U_{eff} = 3.0 eV was used. For structural relaxation and electronic structure calculation, k meshes were set as $11 \times 11 \times 1$ and $33 \times 33 \times 1$, respectively. The criteria for energy and atom force convergence were set to 10^{-5} eV and 0.01 eV Å^{-1}, respectively. The Berry curvatures of the bilayer RuClF were calculated by using the maximally localized Wannier functions (MLWFs)[36,37] implemented in the WANNIER90 package.[38] The energy barrier of sliding FE switching was calculated by the climbing image nudged elastic band (CI-NEB) method.[39]

3. Results and discussion

The proposed mechanism originates from monolayer hexagonal lattices that exhibit spontaneous valley polarization. These systems typically exhibit FM exchange interaction with either the time-reversal (T) or inversion symmetry (P) broken. Subsequently, we constructed bilayer systems by stacking two hexagonal lattices. In the bilayer lattice, antiferromagnetism typically prevails in the interlayer exchange interaction due to competition among various interlayer orbital hybridizations. When a small out-of-plane electric polarization is applied, a pronounced Berry curvature of opposite sign is observed in the vicinity of the K-valley and K′-valley. As illustrated in Fig. 1(a),
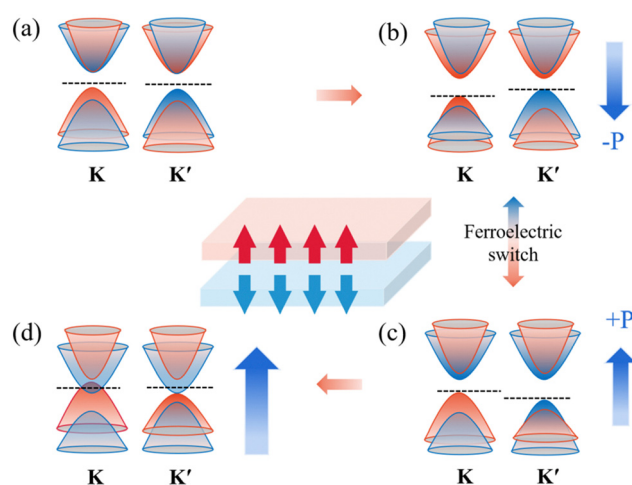

Fig. 1 Schematic diagrams of low-energy conduction bands near the K-valley and K′-valley of a bilayer hexagonal lattice with (a) weak interactions, (b) and (c) two switchable medium electric fields, and (d) a larger electric field. The blue arrow represents the direction of polarization, the red and light-blue arrows in the middle indicate spin-up and spin-down, respectively.

the K-valley and K′-valley come from the spin-up channel in the upper layer and the spin-down channel in the lower layer, respectively. This structure enables layer-locked spin and Berry curvature within the bilayer lattice. As shown in Fig. 1(b)–(d), the P-symmetry of the system is further broken as the applied out-of-plane electric polarization is enhanced, thus lifting the energetic degeneracy between the K and K′ valleys; consequently, it becomes feasible to manipulate the Berry curvature exclusively within a specific layer, paving the way for the realization of AVHE.

Notably, energetically degenerate states with opposite polarization directions can be generated by interlayer sliding or other strategies, as shown in Fig. 1(b) and (c). With FE switching, both the electric polarization and the sign of valley polarization are reversed simultaneously, thus providing the possibility for FE control over the layer-locked physical properties. Moreover, the conduction band minimum (CBM) and valence band maximum (VBM) at the K and K′ valleys intersect or cross to form valley polarization when the out-of-plane electric polarization is further increased, as illustrated in Fig. 1(d).

To validate this hypothesis, we adopted a single-orbit TB model to describe the low-energy band dispersions near the Fermi level in the bilayer hexagonal system. The Hamiltonian for the TB model is formulated as:

$$H = \begin{bmatrix} H_{\mathrm{NN}}^{\mathrm{u}} + H_{\mathrm{NNN}}^{\mathrm{u}} + H_{\mathrm{U}}^{\mathrm{u}} + H_{\mathrm{P}} + H_{\mathrm{onsite}} & 0 \\ 0 & H_{\mathrm{NN}}^{\mathrm{l}} + H_{\mathrm{NNN}}^{\mathrm{l}} + H_{\mathrm{U}}^{\mathrm{l}} - H_{\mathrm{P}} + H_{\mathrm{onsite}} \end{bmatrix},$$

$$(1)$$

where H_{NN} is the nearest-neighbor hopping term modified by

the phase-dependent, capturing the phase-dependent electron transfer, which is expressed as follows:

$$H_{\mathrm{NN}} = \left[e^{i\varphi} \left(e^{i\vec{k}\cdot\vec{r}_1} + e^{i\vec{k}\cdot\vec{r}_2} + e^{i\vec{k}\cdot(\vec{r}_1+\vec{r}_2)} \right) + \mathrm{h.c.} \right] \cdot \begin{pmatrix} t_1 & 0 \\ 0 & t_2 \end{pmatrix}, \quad (2)$$

where r_1 and r_2 are the two nearest-neighbor basis vectors, and t_1 and t_2 are the nearest-neighbor interlayer hopping energies in the spin-up and spin-down, respectively. H_{NNN} is the next-nearest-neighbor hopping term with phase modulation, accounting for longer-range quantum interference:

$$H_{\mathrm{NNN}} = \left(e^{i\vec{k}\cdot\vec{r}_3} + e^{i\vec{k}\cdot\vec{r}_4} + e^{i\vec{k}\cdot(\vec{r}_3+\vec{r}_4)} + \mathrm{h.c.} \right) \cdot \begin{pmatrix} t_3 & 0 \\ 0 & t_4 \end{pmatrix}, \quad (3)$$

where r_3 and r_4 are the two next-nearest-neighbor basis vectors, and t_3 and t_4 are the interlayer hopping energies of the next-nearest-neig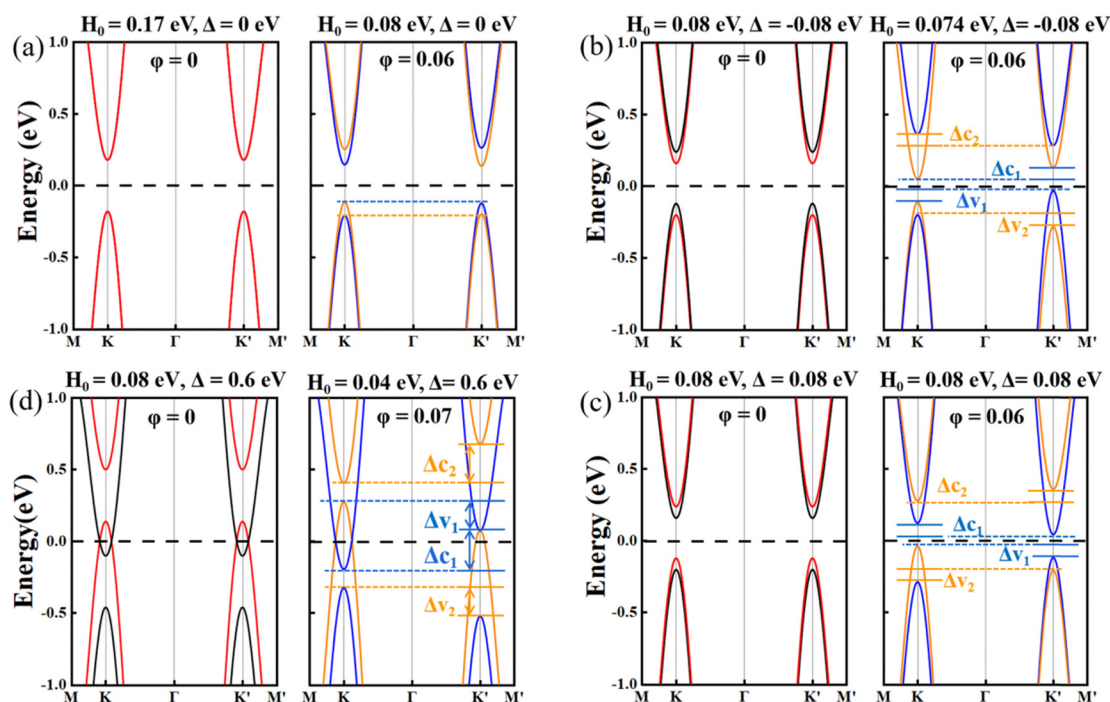hbors in the spin-up and spin-down, respectively. H_{U} is the Hubbard interaction term, describing on-site Coulomb repulsion:

$$H_U = \frac{U}{2} \otimes \sigma_z, \quad (4)$$

where U is the Hubbard interaction of the bilayer hexagonal system.

H_{P} is the out-of-plane electric polarization term, modeling interfacial charge redistribution:

$$H_{\mathrm{P}} = \frac{\Delta}{2} \otimes \sigma_0. \quad (5)$$

Fig. 2 Low-energy conduction bands around the K and K′ valleys of a bilayer hexagonal lattice with (a) weak interaction, (b) and (c) two switchable medium electric fields, and (d) a larger electric field obtained from the TB model, where H_{o} represents the on-site potential energy, Δ represents the imposition of electric polarization, and φ represents the geometric phase applied to the nearest-neighbor hopping. The valley splitting at the CBM is labeled Δc, and the valley splitting at the VBM is Δv.

There is an energy shift of $+\Delta/2$ for lower layer, and $-\Delta/2$ for the upper layer. H_{onsite} is the on-site potential energy:

$$H_{onsite} = t_0 \otimes \sigma_0. \tag{6}$$

The low-energy band dispersions around the K and K′ valleys obtained using the TB model are shown in Fig. 2. The presence of on-site energy (H_{onsite}) and geometric phase (φ) breaks *T*-symmetry and *P*-symmetry, leading to the presence of valley polarization. As illustrated in Fig. 2(a)–(d), the electronic property shifts from semiconductor to BMHM as the electric polarization increases. Notably, at an electric polarization of 0.08, the geometric phase induces a reversal of valley polarization under opposite polarization value, as shown in the Fig. 2(b) and (c). As expected, the TB results are consistent with the proposed model, thus confirming that the mechanism for the layer-polarization-engineered AVHE is feasible.

By using density functional theory, we found a realistic Janus multiferroic system that verifies this mechanism, namely, bilayer RuClF. Fig. 3(a) and Fig. S1(b) (ESI†) show the crystal structure of the monolayer of Janus RuClF, which consists of three atomic layers, with the upper and lower atomic layers occupied by Cl and F atoms, respectively, and the transition metal Ru atoms sandwiched in the middle layer. As the analogue Janus MoSSe (WSSe) monolayer has been obtained in experiments,[40,41] it is expected that the RuClF monolayer can also be fabricated with similar methods. The monolayer RuClF has a hexagonal lattice with the space group $P3m1$, and the optimized lattice constant is 3.30 Å, which is in agreement with a previous study (3.34 Å).[42] The ground state of monolayer RuClF is the FM order, which is energetically more favorable than the AFM state by 0.61 eV, as

shown in Fig. S1(b) in ESI,† with the magnetic moment of $4.0\mu_B$ per unit cell. The band structure of the RuClF monolayer is shown in Fig. S1(a) (ESI†), which is a direct bandgap FM semiconductor with the bandgap of 0.36 eV. After considering the spin–orbit coupling (SOC) effect, the VBM is located at the high-symmetry K point, which is higher than that of point K′, resulting in an obvious valley polarization of 0.29 eV, as illustrated in Fig. S1(c) and (d) (ESI†), which show the band structures of the RuClF monolayer considering SOC with the magnetization along z and $-z$ direction, respectively.

Then, the physical behaviors dependent on the stacking orders of bilayer RuClF were studied. Three types of interlayer contact faces (FRuCl–ClRuF, ClRuF–FRuCl, and FRuCl–FRuCl with Cl–Cl, F–F, and Cl–F interfacing), and three kinds of stacking patterns, stack-I, stack-II, stack-III, were considered, as shown in Fig. 3(d)–(l). The binding energy of bilayer RuClF is defined as follows:

$$E_b = E_{BL} - 2 \times E_{RuClF}, \tag{7}$$

where E_{BL} and E_{RuClF} are the energies of the bilayer and monolayer RuClF per unit cell, respectively, and the calculated E_b values are summarized in Fig. 3(b) and Table S1 (ESI†). As the E_b values of all the structures are negative, the stacking of bilayer RuClF is energetically stable, similar to that of bilayer graphene,[43] bilayer MoS_2[44] and InN/VSi_2P_4 heterostructure.[45] Among them, the systems with stack-II and stack-III configurations have nearly degenerate energies, which are slightly lower than those in stack-I configuration. The variations in interlayer distance (the minimum distance along the z direction between the atomic interfaces in two RuClF sublayers) of the bilayer RuClF are plotted in Fig. 3(c) and Table S2 (ESI†). Here, the
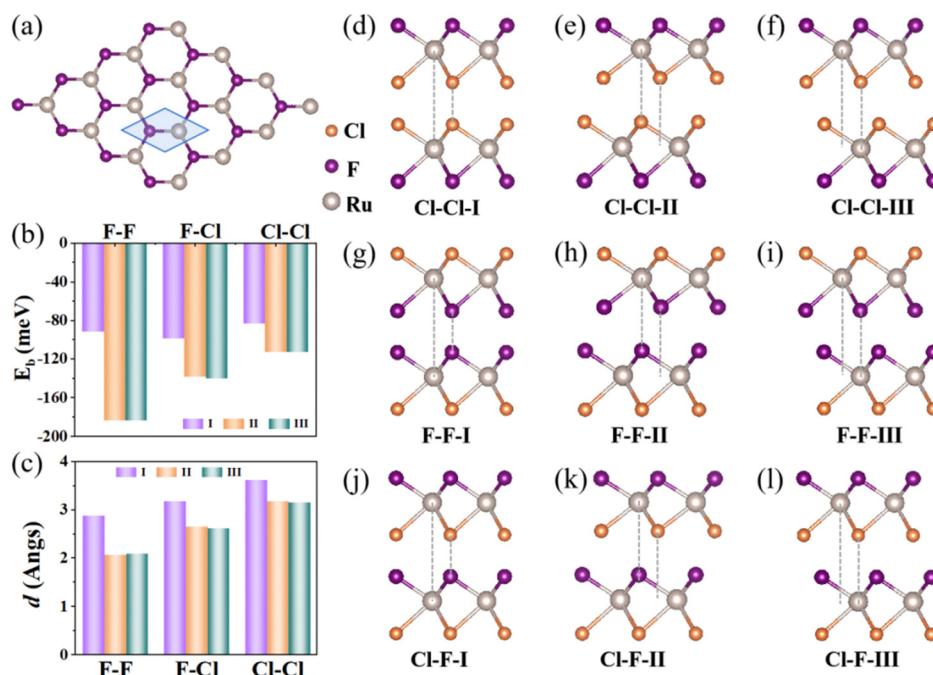

Fig. 3 (a) Top view of the Janus RuClF monolayer. The blue area represents the unit cell of the RuClF monolayer. (b) Binding energy and (c) interlayer distance between RuClF bilayers. (d)–(l) Side views of bilayer RuClF with different stacking orders (stack-I, stack-II, stack-III) and interfaces (FRuCl–ClRuF, ClRuF–FRuCl, and FRuCl–FRuCl).

stack-II and stack-III configurations exhibit smaller interlayer distances, according well with their larger interlayer interactions. Moreover, to confirm the magnetic ground state of bilayer RuClF, the FM state and the interlayer AFM state of nine configurations are compared in Table S3 (ESI†), and the results show that the interlayer AFM order is the most favorable magnetic state for all RuClF bilayers.

Next, the electronic properties of interlayer AFM RuClF bilayers with different configurations were explored. First of all, the band structures of three stacked FRuCl–ClRuF configurations without and with SOC effect are shown in Fig. 4(a)–(f). For the bilayer FRuCl–ClRuF with Cl–Cl interface, the interlayer interactions are weak due to the relatively small electronegativity of Cl atoms. As a result, the spin-up and spin-down bands of the Cl–Cl-I, Cl–Cl-II and Cl–Cl-III configurations completely overlap without considering the SOC effect, as shown in Fig. 4(a)–(c). After considering SOC, spontaneous valley polarization of the RuClF monolayer is induced due to breaking of the T-symmetry. Due to the direct overlap of two RuClF sublayers, no global energy polarization appears at the K and K′ valleys (see Fig. 4(d)–(f)). By doping the holes, spin-up and spin-down holes at K and K′ valleys will be aggregated on the left side of the upper layer and on the right side of the lower layer by applying in-plane electric field, resulting in the layer-locked spin and Berry curvature in the bilayer lattice.

Fig. 5(a)–(c) show the energy band structures of the ClRuF–FRuCl configurations in three stacks without and with considering SOC effects. For the F–F-I stacking with P-symmetry, the bands of spin-up and spin-down channels are completely

degenerate (see Fig. 5(a)). As for F–F-II and F–F-III stacked bilayers, they are bipolar magnetic semiconductors (BMS) with a direct bandgap of 21.55 meV. By considering the SOC effect, the two RuClF sublayers in F–F-I stacks are valley polarized, but the energies at the K-valley and K′-valley are degenerate, originating from the upper and lower RuClF layers, respectively. Differently, global valley polarization occurs in the case of F–F-II and F–F-III stacks under the SOC effect. For the former, the VBM comes from the spin-up channel of the upper layer with a valley polarization value of $\Delta v = 68.7$ meV $\left(\Delta v = E_v^K - E_v^{K'}\right)$. For the latter, the VBM comes from the spin-down channel of the lower layer, and the valley polarization value is around $\Delta v = -68.7$ meV. All the results indicate that the electronic properties of the valley are significantly influenced by the layer-locked Berry curvature.

Moreover, when sliding from F–F-II stack to F–F-III stack, the ClRuF–FRuCl bilayer displays electric polarization featuring two switchable FE states. The out-of-plane electric polarizations under F–F-II and F–F-III stack configurations are 5×10^{-12} C m^{-1} and -5×10^{-12} C m^{-1}, respectively, as calculated by the Berry phase approach. The feasibility of such sliding ferroelectricity is evaluated by the NEB method, and the calculated energy barrier is about 30 meV (see Fig. 5(d)), which is comparable with that in bilayer VSi$_2$P$_4$,[46] suggesting the sliding between RuClF bilayers is energetically possible. The Berry curvatures for the two configurations are shown in Fig. 5(e) and Fig. S2 (ESI†), which is defined as:[47]

$$\Omega(k) = -\sum_n \sum_{n \neq n'} f(n) \frac{2\mathrm{Im}\langle \varphi_{nk}|v_x|\varphi_{n'k}\rangle\langle\varphi_{n'k}|v_y|\varphi_{nk}\rangle}{(E_n - E_{n'})^2}, \quad (8)$$
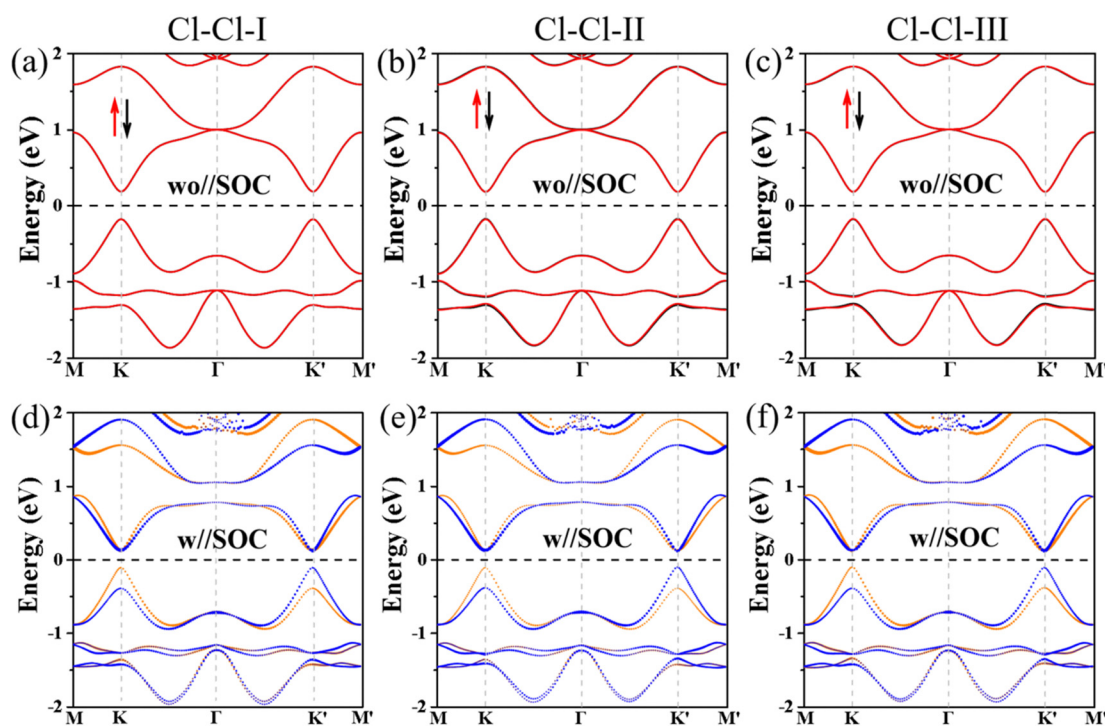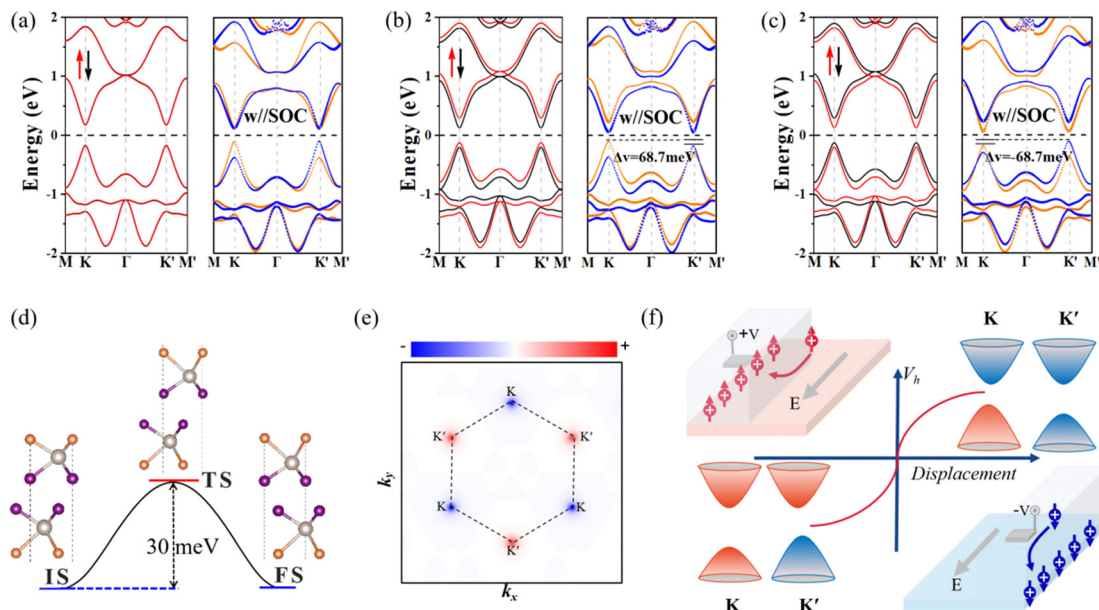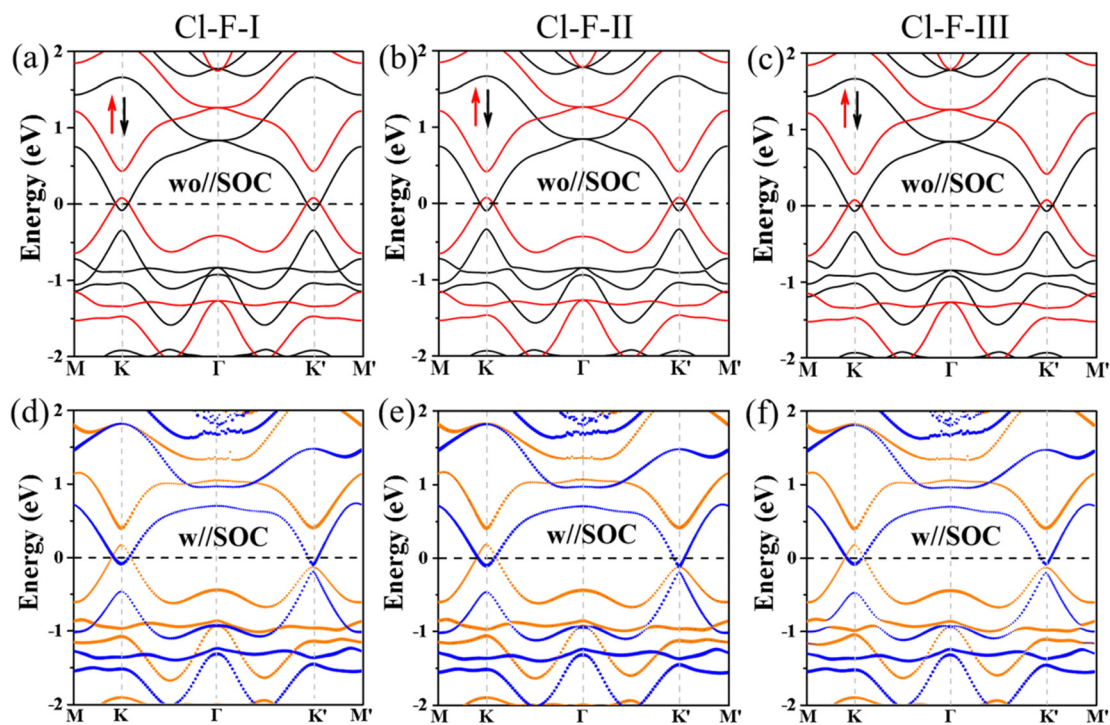

Fig. 4 Band structures of the FRuCl–ClRuF bilayer in the Cl–Cl-I, Cl–Cl-II, and Cl–Cl-III stacking configurations (a)–(c) without and (d)–(f) with SOC effects. The red and black arrows represent spin-up and spin-down channels, and the orange and blue dotted lines represent contributions from the upper and lower RuClF layers, respectively.

Fig. 5 (a)–(c) Band structures of the ClRuF–FRuCl bilayer in F–F-I, F–F-II, and F–F-III without and with SOC effects. The left and right panels show the band structures without and with SOC effect, respectively. Red and black arrows represent spin-up and spin-down channels, respectively. Orange and blue dotted lines represent contributions from the upper and lower RuClF layer, respectively. (d) Sliding energy barrier of bilayer RuClF from F–F-II to F–F-III stack configuration. (e) Berry curvature of the F–F-II stack ClRuF–FRuCl bilayer. (f) Diagrams illustrating the layer-polarized AVHE for stack-II and stack-III RuClF bilayer with the F–F oriented bilayer ClRuF–FRuCl under hole doping.

where n is the band indexes, and $f(n)$, $v_x(v_y)$, and $|\phi_{nk}\rangle$ are the Fermi–Dirac distribution function, the velocity operator along the x/y direction, and the periodic part of the Bloch wave function with eigenvalue E_n, respectively. It is shown that the Berry curvature at the K (K′) valley has a large negative (positive) value for the stack-II (stack-III) ClRuF–FRuCl bilayer. As the layer-locked Berry curvature

Fig. 6 Band structures of the FRuCl–FRuCl bilayer in the F–Cl-I, F–Cl-II, and F–Cl-III stack configurations without (a)–(c) and with (d)–(f) SOC effects. The red and black arrows represent spin-up and spin-down channels; the orange and blue dotted lines represent contributions from upper and lower RuClF layers, respectively.

in the stack-II configuration has strong influence on the electronic properties, in this case, the Fermi level is shifted downward upon hole doping, and the spin-up holes in the K valley would acquire an anomalous velocity $v \approx -\frac{e}{\hbar} E \times \Omega(k)$ under an in-plane electric field and accumulate at the left side of the upper layer. By reversing the FE polarization direction to the stack-III direction through sliding, the spin-down holes in the K′ valley will acquire opposite anomalous velocity and accumulate on the right side of the lower layer because of the opposite Berry curvature, generating the ferroelectrically reversible layer-polarized AVHE (see Fig. 5(f)).

The band structures of the Cl–F oriented FRuCl-FRuCl bilayer without/with considering SOC effect are shown in Fig. 6(a)–(f). It is observed that the three stack configurations (stack-I, stack-II, stack-III) show the same electronic structures, in which both spin-up conduction bands and spin-down valence bands cross the Fermi level and form a metallic state. Particularly, the conducting channels are layer dependent, *i.e.*, the upper RuClF layer conducts in the spin-up channel, while the lower RuClF layer conducts in the spin-down channel. Such spin filter character is referred to as BMHM. Unlike the traditional FM half-metal, which has only one spin-conducting channel, BMHM can attain spin flows with different directions in different layers.

4. Conclusions

By combining the tight-binding (TB) model and first-principles calculations, we propose a mechanism for engineering layer-polarized electronic properties through the coupling of out-of-plane ferroelectricity and A-type AFM ordering in vdW Janus bilayers. Our analysis reveals that the F–F interlayer termination in bilayer RuClF hosts a layer-locked Berry curvature and enables layer-polarized AVHE. Furthermore, the layer-polarized AVHE exhibits ferroelectrically reversible switching upon sliding the two RuClF sublayers. Additionally, the electronic properties of the RuClF bilayer are highly sensitive to stacking configurations. These findings establish a feasible approach for manipulating layer-polarized electronic states in realistic bilayer materials.

Data availability

The data supporting this article have been included as part of the ESI.†

Conflicts of interest

There are no conflicts to declare.

Acknowledgements

References

1 J. W. Chu, Y. Wang, X. P. Wang, K. Hu, G. F. Rao, C. H. Gong, C. C. Wu, H. Hong, X. F. Wang, K. H. Liu, C. L. Gao and J. Xiong, *Adv. Mater.*, 2021, **33**, 2004469.

2 C. B. Luo, Z. Y. Huang, H. Qiao, X. Qi and X. P. Peng, *J. Phys. Mater.*, 2024, **7**, 022006.

3 R. C. G. Naber, K. Asadi, P. W. M. Blom, D. M. de Leeuw and B. de Boer, *Adv. Mater.*, 2010, **22**, 933.

4 R. C. G. Naber, C. Tanase, P. W. M. Blom, G. H. Gelinck, A. W. Marsman, F. J. Touwslager, S. Setayesh and D. M. de Leeuw, *Nat. Mater.*, 2005, **4**, 243.

5 Y. Y. Gao, M. Y. Gao and Y. R. Lu, *Nanoscale*, 2021, **13**, 19324.

6 N. A. Hill, *J. Phys. Chem. B*, 2000, **104**, 6694.

7 N. A. Hill and A. Filippetti, *J. Magn. Magn. Mater.*, 2002, **242**, 976.

8 R. J. K. Barik, S. Mishra, M. Khazaei, S. Y. Wang, Y. Y. Liang, Y. Sun, A. Ranjbar, T. L. Tan, J. J. Wang, S. J. Yunoki, K. Ohno, Y. Kawazoe and A. K. Singh, *Nano Lett.*, 2024, **24**, 13213.

9 D. I. Khomskii, *J. Magn. Magn. Mater.*, 2006, **1**, 1.

10 J. Wang, J. B. Neaton, H. Zheng, V. Nagarajan, S. B. Ogale, B. Liu, D. Viehland, V. Vaithyanathan, D. G. Schlom, U. V. Waghmare, N. A. Spaldin, K. M. Rabe, M. Wuttig and R. Ramesh, *Science*, 2003, **299**, 1719.

11 W. Chen, Z. Sun, Z. Wang, L. Gu, X. Xu, S. Wu and C. Gao, *Science*, 2019, **366**, 983.

12 Y. Xu, A. Ray, Y. T. Shao, S. Jiang, K. Lee, D. Weber, J. E. Goldberger, K. Watanabe, T. Taniguchi, D. A. Muller, K. F. Mak and J. Shan, *Nat. Nanotechnol.*, 2022, **17**, 143.

13 X. Li, X. Xu, H. Zhou, H. Jia, E. Wang, H. Fu, J. T. Sun and S. Meng, *Nano Lett.*, 2023, **23**, 2839.

14 W. Xun, C. Wu, H. Sun, W. Zhang, Y.-Z. Wu and P. Li, *Nano Lett.*, 2024, **24**, 3541.

15 Z. M. Yu, S. Guan, X. L. Sheng, W. Gao and S. S. A. Yang, *Phys. Rev. Lett.*, 2020, **124**, 037701.

16 D. Chen, Z. Lian, X. Huang, Y. Su, M. Rashetnia, L. Yan, M. Blei, T. Taniguchi, K. Watanabe and S. Tongay, *Nat. Commun.*, 2022, **13**, 4810.

17 L. Liu, J. H. Hua, X. Zhang, M. H. Lu and Y. F. Chen, *Phys. Rev. Appl.*, 2023, **19**, 044055.

18 C. Wang, X. Zhou, Y. Pan, J. Qiao, X. Kong, C. C. Kaun and W. Ji, *Phys. Rev. B*, 2018, **97**, 245409.

19 C. Wang, X. Zhou, L. Zhou, Y. Pan, Z. Y. Lu, X. Wan, X. Wang and W. Ji, *Phys. Rev. B*, 2020, **102**, 020402(R).

20 T. Guo, Y. Liu, Y. Sun, S. Zhang, X. Xu, L. Wang, W. Zhou, Y. Liu, X. Yao and X. Zhang, *Appl. Phys. Lett.*, 2023, **122**, 192403.

21 W. Xun, X. Liu, Y. Zhang, Y.-Z. Wu and P. Li, *Appl. Phys. Lett.*, 2025, **126**, 161903.

22 K. Yasuda, X. Wang, K. Watanabe, T. Taniguchi and P. JarilloHerrero, *Science*, 2021, **372**, 1458.

23 S. Deb, W. Cao, N. Raab, K. Watanabe, T. Taniguchi, M. Goldstein, L. Kronik, M. Urbakh, O. Hod and M. Ben Shalom, *Nature*, 2022, **612**, 465.

24 L. Rogee, L. Wang, Y. Zhang, S. Cai, P. Wang, M. Chhowalla, W. Ji and S. P. Lau, *Science*, 2022, **376**, 973.

25 X. Wang, K. Yasuda, Y. Zhang, S. Liu, K. Watanabe, T. Taniguchi, J. Hone, L. Fu and P. Jarillo-Herrero, *Nat. Nanotechnol.*, 2022, **17**, 367.

26 C. Wu, H. Sun, P. Dong, Y.-Z. Wu and P. Li, *Adv. Funct. Mater.*, 2025, **35**, 2501506.

27 X. Han, J. Y. You, S. Wu, R. Li, Y. P. Feng, K. P. Loh and X. Zhao, *J. Am. Chem. Soc.*, 2023, **145**, 3624.

28 D. Dai, B. Fu, J. Yang, L. Yang, S. Yan, X. Chen, H. Li, Z. Zuo, C. Wang, K. Jin and Q. Gong, *Sci. Adv.*, 2024, **10**, 1281.

29 Y. Wu, J. Tong, L. Deng, F. Luo, F. Tian, G. Qin and X. Zhang, *Nano Lett.*, 2023, **23**, 6226.

30 G. Kresse and J. Furthmuller, *Mater. Sci.*, 1996, **6**, 15.

31 G. Kresse and J. Hafner, *Phys. Rev. B: Condens. Matter Mater. Phys.*, 1993, **48**, 13115.

32 J. P. Perdew, K. Burke and M. Ernzerhof, *Phys. Rev. Lett.*, 1996, **77**, 3865.

33 P. E. Blochl, *Phys. Rev. B: Condens. Matter Mater. Phys.*, 1994, **50**, 17953.

34 S. Grimme, *J. Comput. Chem.*, 2004, **25**, 1463.

35 S. Grimme, *J. Comput. Chem.*, 2006, **27**, 1787.

36 A. A. Mostofi, J. R. Yates, G. Pizzi, Y. S. Lee, I. Souza, D. Vanderbilt and N. Marzari, *Comput. Phys. Commun.*, 2014, **185**, 2309.

37 X. Kong, L. Li, O. Leenaerts, X. J. Liu and F. M. Peeters, *Phys. Rev. B*, 2017, **96**, 035123.

38 A. A. Mostofi, J. R. Yates, Y. S. Lee, I. Souza, D. Vanderbilt and N. Marzari, *Comput. Phys. Commun.*, 2008, **178**, 685.

39 G. Mills, H. Jónsson and G. Schenter, *Surf. Sci.*, 1995, **324**, 305.

40 J. Zhang, S. Jia, I. Kholmanov, L. Dong, D. Er, W. Chen, H. Guo, Z. Jin, V. B. Shenoy, L. Shi and J. Lou, *ACS Nano*, 2017, **11**, 8192.

41 D. B. Trivedi, G. Turgut, Y. Qin, M. Y. Sayyad, D. Hajra, M. Howell, L. Liu, S. Yang, N. H. Patoary, H. Li, M. M. Petrić, M. Meyer, M. Kremser, M. Barbone, G. Soavi, A. V. Stier, K. Müller, S. Yang, I. S. Esqueda, H. Zhuang, J. J. Finley and S. Tongay, *Adv. Mater.*, 2020, **32**, 2006320.

42 Y. B. Ma, Y. Z. Wu, J. W. Tong, L. Deng, X. Yin, L. Q. Zhou, X. L. Han, F. B. Tian and X. M. Zhang, *Nanoscale*, 2023, **15**, 8278.

43 E. Mostaani, N. D. Drummond and V. I. Falko, *Phys. Rev. Lett.*, 2015, **115**, 115501.

44 Z. Wang, Q. Chen and J. Wang, *J. Phys. Chem. C*, 2015, **119**(9), 4752.

45 Y. Zhu, M. Su, H. Ye, D. Bai and J. Wang, *Phys. Rev. B*, 2023, **108**, 125413.

46 T. Zhang, X. L. Xu, B. B. Huang, Y. Dai, L. Z. Kou and Y. D. Ma, *Mater. Horiz.*, 2023, **10**, 483.

47 D. J. Thouless, M. Kohmoto, M. P. Nightingale and M. den Nijs, *Phys. Rev. Lett.*, 1982, **49**, 405.